Cite as: Y. Zhong *et al.*, *Science* 10.1126/science.aax9385 (2019).

Wafer-scale synthesis of monolayer two-dimensional porphyrin polymers for hybrid superlattices

Yu Zhong[1]*, Baorui Cheng[1]*, Chibeom Park[1,2], Ariana Ray[3], Sarah Brown[1,2], Fauzia Mujid[1], Jae-Ung Lee[4,5], Hua Zhou[6], Joonki Suh[1], Kan-Heng Lee[4,7], Andrew J. Mannix[2], Kibum Kang[1,2,8], S. J. Sibener[1,2], David A. Muller[7], Jiwoong Park[1,2,4]†

[1]Department of Chemistry, University of Chicago, Chicago, IL 60637, USA. [2]James Franck Institute, University of Chicago, Chicago, IL 60637, USA. [3]Department of Physics, Cornell University, Ithaca, NY 14853, USA [4]Pritzker School of Molecular Engineering, University of Chicago, Chicago, IL 60637, USA. [5]Department of Physics, Ajou University, Suwon 16499, Republic of Korea. [6]Advanced Photon Source, Argonne National Laboratory, Lemont, IL 60439, USA. [7]School of Applied and Engineering Physics, Cornell University, Ithaca, NY 14853, USA. [8] Department of Materials Science and Engineering, Korea Advanced Institute of Science and Technology (KAIST), Daejeon 34141, Republic of Korea.

*These authors contributed equally to this work. †Corresponding author. Email: jwpark@uchicago.edu

The large-scale synthesis of high-quality thin films with extensive tunability derived from molecular building blocks will advance the development of artificial solids with designed functionalities. We report the synthesis of two-dimensional (2D) porphyrin polymer films with wafer-scale homogeneity in the ultimate limit of monolayer thickness by growing films at a sharp pentane/water interface, which allows the fabrication of their hybrid superlattices. Laminar assembly polymerization of porphyrin monomers could form monolayers of metal-organic frameworks with Cu^{2+} linkers or covalent organic frameworks with terephthalaldehyde linkers. Both the lattice structures and optical properties of these 2D films were directly controlled by the molecular monomers and polymerization chemistries. The 2D polymers were used to fabricate arrays of hybrid superlattices with MoS_2 that could be used in electrical capacitors.

Monolayer 2D polymers (2DPs), which are one-molecule-thick, freestanding films comprised of periodically linked monomers (*1–4*), offer an ideal material system with two key advantages. First, their properties can be tuned at the molecular level by using different monomers and polymerization chemistries (*5*, *6*). Second, as the molecular analogs of 2D atomic crystals (*e.g.* graphene and transition metal dichalcogenides (TMDs)) (*7–9*), 2DPs can be assembled through van der Waals (vdW) interactions into heterostructures and superlattices layer-by-layer. Van der Waals heterostructures generated from 2D atomic crystals have produced properties not observed in individual building blocks (*10*, *11*). Adding the chemical tunability of the 2DPs to such vdW heterostructures will lead to the properties and functionalities that are designed at the molecular level and further tuned by the interlayer interactions. However, it has remained an unmet challenge to scalably synthesize monolayer 2DP films and subsequently integrate them with other materials with monolayer precision (*12*, *13*). This is due to the difficulty of controlling reactions in the monolayer limit with large scale uniformity and the lack of facile methods for the transfer and integration of monolayer 2DPs because of their fragility. Previous experiments have reported progress toward large-scale synthesis of 2DPs (*14–22*), but with limited success with regard to wafer-scale homogeneity, microscopic characterization of crystalline structures, and scalable thin-film integration (*23*).

Here, we report the wafer-scale synthesis and integration of monolayer 2DPs for the fabrication of their hybrid heterostructures with monolayer precision. We developed an interfacial synthesis technique, laminar assembly polymerization (LAP), that is compatible with various molecular building blocks and two primary polymerization chemistries (coordination and covalent). This approach incorporated key features necessary for scalable and facile processing, including large-area synthesis, ambient growth conditions, and compatibility with established patterning and integration methods. These characteristics enabled the fabrication of superlattices based on monolayer 2DPs and 2D atomic crystals.

The design approach for the 2DP monolayers was based on porphyrin building blocks (Fig. 1A). These molecules have two variation sites — one at the center of the porphyrin ring (**M** = 2H, Fe(III), or Pt(II)) that tuned the optical spectra (Fig. 1B) and the other on the phenyl groups (**R** = -COOH or $-NH_2$) that controlled the monomer-monomer bonds. The monomers crosslinked either through coordination bonds via a copper paddle wheel structure in the presence of Cu^{2+} ions (left, Fig. 1A and fig. S1; **R** = -COOH) (*14*), or through covalent bonds via the Schiff base reaction in the presence of terephthalaldehyde (TPA) (right, Fig. 1A and fig. S1; **R** = $-NH_2$) (*21*). The former forms coordination 2DPs (**2DP I-III**, **M** = 2H, Pt^{2+} or Fe^{3+}, respectively), also known as monolayer metal-organic frameworks (MOFs), whereas the latter forms covalent

2DPs (**2DP IV**, **M** = 2H), also known as monolayer covalent organic frameworks (COFs). The linkage chemistry for all the 2DPs were confirmed by Fourier-transform infrared spectroscopy (FTIR) (fig. S2).

Wafer-scale 2DP films were all produced at a sharp pentane-water interface and then transferred onto a substrate (*e.g.* fused silica in Fig. 1) placed underneath by slowly draining the bottom solution (more details in the supplementary text). We visualized these films using a custom color-coding scheme based on the hyperspectral optical transmission images (Fig. 1C and fig. S3). Images of four transferred 2DP monolayers that covered an entire 2-inch (5-cm) fused silica substrate are shown in Fig. 1D. The films displayed uniform contrast over entire wafers, suggesting macroscopic continuity and homogeneity (higher resolution analysis shown in fig. S4). The MOF-based **2DP I-III** with different **M** had distinct absorption spectra (Fig. 1B), resulting in markedly different colors shown in Fig. 1D. The absorption spectra of the 2DPs resembled those of the corresponding porphyrin monomers (figs. S5 and S6, discussions in the supplementary text), indicating that the optical properties of the 2DP films could be directly tuned at the molecular level.

These monolayer 2DPs were synthesized using LAP explained in Fig. 2. It is based on monomer self-assembly and polymerization at the sharp interface formed between two immiscible solvents (pentane/water) that strictly confined the monomers in a monolayer limit, which was critical for precise control of the thickness (Fig. 2, A and B). Laminar flow of the assembled monomers led to large-scale continuity and homogeneity in thickness (Fig. 2A and fig. S7 describe the LAP synthesis and the in situ optical characterization apparatus; additional details in the supplementary text).

There are three phases in the LAP process (illustrated in Figs. 2A and 2B): injection, self-assembly, and polymerization. During injection, the monomers were introduced from the edge of the reactor (width *W*) and directly delivered onto the sharp pentane/water interface by a continuous stream of carrier solution through the pentane layer (within 1 cm from the edge, Movie S1). The pentane-mediated delivery has two key advantages. First, the mass flow of the precursor is continuous at the interface, which is achieved by using microsyringe pumps and by carefully choosing the combination of the carrier solvents. Second, the pentane/water interface is steady during the growth, resulting in minimal disturbance. This contrasts with dropwise delivery through the air, which disturbs the interface. Once delivered to the interface, the porphyrin-based monomers self-assembled at the interface because of their amphiphilicity and then spread, while being restricted by the longer sidewalls (length *L*). This process generated laminar flow of the monomers away from the injection region and resulted in a continuous monolayer assembly. Then, the polymerization of assembled monomers takes place gradually through the reaction with the reagents present in water (Cu^{2+} ions for MOF-based **2DP I-III**; TPA for COF-based **2DP IV**).

The monolayer nature of the 2DPs was confirmed by optical images that showed unidirectional movement of the monolayer assembly parallel to the longer sidewalls (Fig. 2C; see Movie S2) with little mixing perpendicular to this direction (Fig. 2F), confirming a laminar flow. This monolayer remained intact upon solvent washing after a complete polymerization (~30 min); in contrast, unpolymerized films were washed away (Fig. 2D). Quantitative measurements of the synthesized area of **2DP I** (**R** = -COOH and **M** = 2H with Cu^{2+} ions) as a function of the injected volume of the monomer solution closely followed a linear growth model consistent with a near-unity monomer-to-monolayer yield (Fig. 2E and Movie S3).

The LAP synthesis offers several advantages important for thin-film processing and integration of 2DP monolayers. First, the growth can be easily scaled up by injecting more monomers (for larger *L*) and by adding an array of nozzles in parallel (for larger *W*) (fig. S8). For example, the 2-inch films shown in Fig. 1D were synthesized with three nozzles in a 2" (*W*) by 5" (*L*) reactor. Second, lateral heterojunctions of monolayer 2DPs can be grown with tunable compositions and widths by introducing different monomers from each nozzle and by controlling the relative injection rates (Fig. 2, F and G, and fig. S9). Sharp interfaces between adjacent monolayer stripes were observed without voids. Finally, the 2DP monolayer films were compatible with a wide range of patterning and transfer techniques. For instance, they can be transferred to various substrates without tearing, distortion or buckling after evaporating pentane (*e.g.* SiO_2/Si in Fig. 3B and gold in Fig. 3D), and they could be patterned by using a laser marker while still on the water surface with a scanning laser (fig. S10). Multiple patterning and transfer steps can be combined to fabricate laterally-patterned and vertically-stacked heterostructures while maintaining the integrity of the intricate patterns, as shown in Fig. 2H and fig. S10.

The 2DP films were mechanically robust and homogeneous in thickness. On the large scale, they exhibited considerable mechanical strength and could be transferred onto various substrates as continuous films, as shown in Fig. 1D. As an additional example, a scanning electron microscopy (SEM) image of a **2DP I** film transferred and suspended over a holey transmission electron microscope (TEM) grid (2 μm diameter holes; Fig. 3A) displays an array of freestanding 2DP membranes. These membranes were suspended with a near perfect yield (> 99%; one broken membrane denoted by an arrow) and appeared uniform and continuous over the entire area without cracks or voids. These 2DP films were close to 1 nm in height, near the expected thickness of a monolayer (*24*), with a uniform and smooth surface as measured by

atomic force microscopy (Fig. 3B and fig. S11).

The MOF-based **2DP I-III** showed polycrystalline structure as confirmed by the synchrotron grazing incidence X-ray diffraction (GIXRD) in Fig. 3C and figs. S12 and S13. Using **2DP II** as an example, the in-plane XRD pattern showed all of the main peaks predicted based on the structure model (inset in Fig. 3C and supplementary table S1) and the average lateral domain size was estimated to be ~20 nm according to Scherrer equation. As additional evidence, the crystalline structure of **2DP II** monolayers transferred onto flat Au(111) surfaces was confirmed with scanning tunneling microscopy (STM) performed under ultra-high vacuum. The STM topography image (Fig. 3D) showed a square lattice with a single-crystalline domain that fully covered the 30 nm by 30 nm area (see the 2D fast Fourier transform (FFT) image; inset in Fig. 3D). Another STM image (Fig. 3E; 60 nm by 60 nm) displayed three primary crystalline orientations (lattice constant a = 1.66 ± 0.03 nm, measured from Fig. 3F), suggesting that the **2DP II** films were polycrystalline with domain structures similar to those in previously imaged 2DPs (*25*, *26*). The lattice constant extracted from these microscopic STM analyses is close to that from GIXRD measurements (1.64 nm) performed on the macroscopic scale (0.1 mm by 10 mm) with a mismatch less than 2% (Fig. 3C and fig. S12 and S13). A composite inverse 2D FFT image (Fig. 3G) has each region colored according to the lattice orientation. We used this map to estimate the size of domains (between 10 and 40 nm) and locate domain boundaries (marked by dashed lines in Fig. 3E). For the COF-based **2DP IV**, no evidence for long-range order could be collected (through GIXRD or selected area electron diffraction), similar to other monolayer covalent 2DPs reported previously (*26*).

In Fig. 4, we further demonstrate the potential of LAP by presenting an array of vertically programmed hybrid vdW superlattices. These superlattices were produced by repeatedly stacking in vacuum hybrid 2D building units 2DP/$(MoS_2)_n$, each made of a 2DP monolayer and n monolayers of MoS_2. Examples of a **2DP II**/$(MoS_2)_3$ superlattice and a **2DP II**/MoS_2 film are shown in Fig. 4, A and B, respectively (detailed methods are shown in figs. S14 and S15) (*27*, *28*). Figure 4A shows a cross-sectional annular dark field (ADF) scanning transmission electron microscope (STEM) image of a representative **2DP II**/$(MoS_2)_3$ superlattice—a 11-layer stack—constructed by alternating one layer of **2DP II** and three layers of MoS_2. The image shows three bright bands separated by two dark lines. Each of the bright bands consisted of three layers of MoS_2 and the dark layer in between corresponds to a **2DP II** monolayer, as confirmed by the composite ADF and electron energy loss spectroscopy (EELS) mapping (Fig. 4A and fig. S16). The films ran parallel to each other with sharp interfaces and uniform layer thickness over the entire 100 nm view of the ADF STEM image, indicating a high level of uniformity. In addition, the composition of the superlattice could be tuned by using a different 2DP, as demonstrated by the **2DP III**/$(MoS_2)_2$ superlattice shown in Fig. 4C. EELS spectra confirmed the chemical composition of each constituting layer, where **2DP III** was identified by a strong carbon signal and MoS_2 by a strong sulfur signal (Fig. 4C and fig. S16).

The vertical structure and composition of the hybrid vdW superlattices could be directly engineered by using different hybrid building units. Figure 4D (left) shows a series of vdW superlattices with varied superlattice periodicity d made of **2DP II**/$(MoS_2)_n$ repeating units, for n = 1, 2, or 3. The grazing incidence wide-angle x-ray scattering (GIWAXS) data presented in Fig. 4D (middle and right) and figs. S17 and S18 show the distinctive diffraction peak for each superlattice. By radially integrating the 2D GIWAXS images along the out-of-plane direction, 1D spectra were obtained in reciprocal space and used to measure d (fig. S19). For example, the superlattice with n = 3 showed d = 3.5 nm and a vdW thickness of 1.5 nm for **2DP II**, near the value measured from Fig. 4A. The results from other superlattices agreed very well with the predicted values (fig. S14 and supplementary table S2). In addition, X-ray reflectivity (XRR) measurements conducted on similar superlattice structures and the scattering length density profiles generated from fitting the XRR spectra clearly reveal the oscillations of electron density consistent with the alternating structures of $(MoS_2)_n$ and **2DP II** (fig. S20 and supplementary text). The thickness of the repeating units extracted from the XRR analysis matches those obtained from GIWAXS and cross-sectional STEM within 2Å mismatch (supplementary table S3). Both the GIWAXS and the XRR data were taken from a macroscopic area randomly chosen from 1 cm by 1 cm superlattice films, illustrating the homogeneity of the vdW superlattices on a large scale.

Vertically programmed vdW superlattices and heterostructures provide a powerful platform for fabricating uniform arrays of devices whose properties are engineered layer by layer (*10*, *11*, *29*–*32*). To demonstrate such potential, we chose to fabricate arrays of electrical capacitors (a photo shown in Fig. 4F) from vdW heterostructures of **2DP II** and MoS_2 (Fig. 4E), as it involves integration of both top and bottom electrodes and the capacitance can be directly tuned by the thickness of the superlattices. Each device in an array consisted of two gold electrodes sandwiching the vdW heterostructure dielectric (*27*). Figure 4G shows the results measured from a series of heterostructures, $(MoS_2/$**2DP II**$)_N(MoS_2)_{6-N}$, where N monolayers of **2DP II** films were inserted in between MoS_2 layers of a 6-layer MoS_2 stack (schematics in Fig. 4G). Thus, the dielectric thickness and the capacitance are directly tuned by varying the layer number of monolayer **2DP II**. The measured inverse capacitance $1/C'$, where C' is the area-normalized capacitance, linearly

increased as N increased from 1 to 5. Using the classical capacitor model, we extracted the dielectric constants of **2DP II** (4.1) and MoS_2 (2.7), in agreement with reported values (*33*, *34*). The measured capacitance from an array of devices exhibited a narrow distribution (lower inset in Fig. 4G), suggesting the spatial uniformity of the hybrid heterostructures. The spatial uniformity is comparable to what has been achieved with stacked MoS_2 films (*27*). Thus, this method offers a general platform to incorporate diverse molecular species into vdW hybrid thin films for functional devices.

REFERENCES AND NOTES

1. M. Servalli, A. D. Schlüter, Synthetic two-dimensional polymers. *Annu. Rev. Mater. Res.* **47**, 361–389 (2017). doi:10.1146/annurev-matsci-070616-124040
2. P. Payamyar, B. T. King, H. C. Öttinger, A. D. Schlüter, Two-dimensional polymers: Concepts and perspectives. *Chem. Commun.* **52**, 18–34 (2016). doi:10.1039/C5CC07381B Medline
3. D. F. Perepichka, F. Rosei, Chemistry. Extending polymer conjugation into the second dimension. *Science* **323**, 216–217 (2009). doi:10.1126/science.1165429 Medline
4. G. Franc, A. Gourdon, Covalent networks through on-surface chemistry in ultra-high vacuum: State-of-the-art and recent developments. *Phys. Chem. Chem. Phys.* **13**, 14283–14292 (2011). doi:10.1039/c1cp20700h Medline
5. H. Furukawa, K. E. Cordova, M. O'Keeffe, O. M. Yaghi, The chemistry and applications of metal-organic frameworks. *Science* **341**, 1230444 (2013). doi:10.1126/science.1230444 Medline
6. P. J. Waller, F. Gándara, O. M. Yaghi, Chemistry of covalent organic frameworks. *Acc. Chem. Res.* **48**, 3053–3063 (2015). doi:10.1021/acs.accounts.5b00369 Medline
7. K. S. Novoselov, D. Jiang, F. Schedin, T. J. Booth, V. V. Khotkevich, S. V. Morozov, A. K. Geim, Two-dimensional atomic crystals. *Proc. Natl. Acad. Sci. U.S.A.* **102**, 10451–10453 (2005). doi:10.1073/pnas.0502848102 Medline
8. K. F. Mak, C. Lee, J. Hone, J. Shan, T. F. Heinz, Atomically thin MoS_2: A new direct-gap semiconductor. *Phys. Rev. Lett.* **105**, 136805 (2010). doi:10.1103/PhysRevLett.105.136805 Medline
9. K. S. Novoselov, A. K. Geim, S. V. Morozov, D. Jiang, Y. Zhang, S. V. Dubonos, I. V. Grigorieva, A. A. Firsov, Electric field effect in atomically thin carbon films. *Science* **306**, 666–669 (2004). doi:10.1126/science.1102896 Medline
10. K. S. Novoselov, A. Mishchenko, A. Carvalho, A. H. Castro Neto, 2D materials and van der Waals heterostructures. *Science* **353**, aac9439 (2016). doi:10.1126/science.aac9439 Medline
11. A. K. Geim, I. V. Grigorieva, Van der Waals heterostructures. *Nature* **499**, 419–425 (2013). doi:10.1038/nature12385 Medline
12. X. Feng, A. D. Schlüter, Towards macroscopic crystalline 2d polymers. *Angew. Chem. Int. Ed.* **57**, 13748–13763 (2018). doi:10.1002/anie.201803456 Medline
13. J. W. Colson, W. R. Dichtel, Rationally synthesized two-dimensional polymers. *Nat. Chem.* **5**, 453–465 (2013). doi:10.1038/nchem.1628 Medline
14. R. Makiura, S. Motoyama, Y. Umemura, H. Yamanaka, O. Sakata, H. Kitagawa, Surface nano-architecture of a metal-organic framework. *Nat. Mater.* **9**, 565–571 (2010). doi:10.1038/nmat2769 Medline
15. R. Dong, T. Zhang, X. Feng, Interface-assisted synthesis of 2d materials: Trend and challenges. *Chem. Rev.* **118**, 6189–6235 (2018). doi:10.1021/acs.chemrev.8b00056 Medline
16. D. Sheberla, L. Sun, M. A. Blood-Forsythe, S. Er, C. R. Wade, C. K. Brozek, A. Aspuru-Guzik, M. Dincă, High electrical conductivity in Ni_3(2,3,6,7,10,11-hexaiminotriphenylene)$_2$, a semiconducting metal-organic graphene analogue. *J. Am. Chem. Soc.* **136**, 8859–8862 (2014). doi:10.1021/ja502765n Medline
17. R. Dong, M. Pfeffermann, H. Liang, Z. Zheng, X. Zhu, J. Zhang, X. Feng, Large-area, free-standing, two-dimensional supramolecular polymer single-layer sheets for highly efficient electrocatalytic hydrogen evolution. *Angew. Chem. Int. Ed.* **54**, 12058–12063 (2015). doi:10.1002/anie.201506048 Medline
18. H. Sahabudeen, H. Qi, B. A. Glatz, D. Tranca, R. Dong, Y. Hou, T. Zhang, C. Kuttner, T. Lehnert, G. Seifert, U. Kaiser, A. Fery, Z. Zheng, X. Feng, Wafer-sized multifunctional polyimine-based two-dimensional conjugated polymers with high mechanical stiffness. *Nat. Commun.* **7**, 13461 (2016). doi:10.1038/ncomms13461 Medline
19. R. Dong, P. Han, H. Arora, M. Ballabio, M. Karakus, Z. Zhang, C. Shekhar, P. Adler, P. S. Petkov, A. Erbe, S. C. B. Mannsfeld, C. Felser, T. Heine, M. Bonn, X. Feng, E. Cánovas, High-mobility band-like charge transport in a semiconducting two-dimensional metal-organic framework. *Nat. Mater.* **17**, 1027–1032 (2018). doi:10.1038/s41563-018-0189-z Medline
20. T. Bauer, Z. Zheng, A. Renn, R. Enning, A. Stemmer, J. Sakamoto, A. D. Schlüter, Synthesis of free-standing, monolayered organometallic sheets at the air/water interface. *Angew. Chem. Int. Ed.* **50**, 7879–7884 (2011). doi:10.1002/anie.201100669 Medline
21. M. Matsumoto, L. Valentino, G. M. Stiehl, H. B. Balch, A. R. Corcos, F. Wang, D. C. Ralph, B. J. Mariñas, W. R. Dichtel, Lewis-acid-catalyzed interfacial polymerization of covalent organic framework films. *Chem* **4**, 308–317 (2018). doi:10.1016/j.chempr.2017.12.011
22. V. Müller, F. Shao, M. Baljozovic, M. Moradi, Y. Zhang, T. Jung, W. B. Thompson, B. T. King, R. Zenobi, A. D. Schlüter, Structural characterization of a covalent monolayer sheet obtained by two-dimensional polymerization at an air/water interface. *Angew. Chem. Int. Ed.* **56**, 15262–15266 (2017). doi:10.1002/anie.201707140 Medline
23. W. Wang, A. D. Schlüter, Synthetic 2D polymers: A critical perspective and a look into the future. *Macromol. Rapid Commun.* **40**, e1800719 (2019). doi:10.1002/marc.201800719 Medline
24. S. Motoyama, R. Makiura, O. Sakata, H. Kitagawa, Highly crystalline nanofilm by layering of porphyrin metal-organic framework sheets. *J. Am. Chem. Soc.* **133**, 5640–5643 (2011). doi:10.1021/ja110720f Medline
25. J. F. Dienstmaier, A. M. Gigler, A. J. Goetz, P. Knochel, T. Bein, A. Lyapin, S. Reichlmaier, W. M. Heckl, M. Lackinger, Synthesis of well-ordered COF monolayers: Surface growth of nanocrystalline precursors versus direct on-surface polycondensation. *ACS Nano* **5**, 9737–9745 (2011). doi:10.1021/nn2032616 Medline
26. L. Cardenas, R. Gutzler, J. Lipton-Duffin, C. Fu, J. L. Brusso, L. E. Dinca, M. Vondráček, Y. Fagot-Revurat, D. Malterre, F. Rosei, D. F. Perepichka, Synthesis and electronic structure of a two dimensional π-conjugated polythiophene. *Chem. Sci.* **4**, 3263 (2013). doi:10.1039/c3sc50800e
27. K. Kang, K.-H. Lee, Y. Han, H. Gao, S. Xie, D. A. Muller, J. Park, Layer-by-layer assembly of two-dimensional materials into wafer-scale heterostructures. *Nature* **550**, 229–233 (2017). doi:10.1038/nature23905 Medline
28. K. Kang, S. Xie, L. Huang, Y. Han, P. Y. Huang, K. F. Mak, C.-J. Kim, D. Muller, J. Park, High-mobility three-atom-thick semiconducting films with wafer-scale homogeneity. *Nature* **520**, 656–660 (2015). doi:10.1038/nature14417 Medline
29. Y. Liu, Y. Huang, X. Duan, Van der Waals integration before and beyond two-dimensional materials. *Nature* **567**, 323–333 (2019). doi:10.1038/s41586-019-1013-x Medline
30. Y. Liu, N. O. Weiss, X. Duan, H.-C. Cheng, Y. Huang, X. Duan, Van der Waals heterostructures and devices. *Nat. Rev. Mater.* **1**, 16042 (2016). doi:10.1038/natrevmats.2016.42
31. D. Jariwala, T. J. Marks, M. C. Hersam, Mixed-dimensional van der Waals heterostructures. *Nat. Mater.* **16**, 170–181 (2017). doi:10.1038/nmat4703 Medline
32. C. Wang, Q. He, U. Halim, Y. Liu, E. Zhu, Z. Lin, H. Xiao, X. Duan, Z. Feng, R. Cheng, N. O. Weiss, G. Ye, Y.-C. Huang, H. Wu, H.-C. Cheng, I. Shakir, L. Liao, X. Chen, W. A. Goddard III, Y. Huang, X. Duan, Monolayer atomic crystal molecular superlattices. *Nature* **555**, 231–236 (2018). doi:10.1038/nature25774 Medline
33. X. Chen, Z. Wu, S. Xu, L. Wang, R. Huang, Y. Han, W. Ye, W. Xiong, T. Han, G. Long, Y. Wang, Y. He, Y. Cai, P. Sheng, N. Wang, Probing the electron states and metal-insulator transition mechanisms in molybdenum disulphide vertical heterostructures. *Nat. Commun.* **6**, 6088 (2015). doi:10.1038/ncomms7088 Medline
34. E. Redel, Z. Wang, S. Walheim, J. Liu, H. Gliemann, C. Wöll, On the dielectric and optical properties of surface-anchored metal-organic frameworks: A study on epitaxially grown thin films. *Appl. Phys. Lett.* **103**, 091903 (2013). doi:10.1063/1.4819836
35. M. Matsumoto, R. R. Dasari, W. Ji, C. H. Feriante, T. C. Parker, S. R. Marder, W. R. Dichtel, Rapid, low temperature formation of imine-linked covalent organic

frameworks catalyzed by metal triflates. *J. Am. Chem. Soc.* **139**, 4999–5002 (2017). doi:10.1021/jacs.7b01240 Medline
36. D. Nečas, P. Klapetek, Gwyddion: An open-source software for SPM data analysis. *Cent. Eur. J. Phys.* **10**, 181–188 (2012).
37. Y. Liu, J. Guo, E. Zhu, L. Liao, S.-J. Lee, M. Ding, I. Shakir, V. Gambin, Y. Huang, X. Duan, Approaching the Schottky-Mott limit in van der Waals metal-semiconductor junctions. *Nature* **557**, 696–700 (2018). doi:10.1038/s41586-018-0129-8 Medline
38. R. W. Havener, C.-J. Kim, L. Brown, J. W. Kevek, J. D. Sleppy, P. L. McEuen, J. Park, Hyperspectral imaging of structure and composition in atomically thin heterostructures. *Nano Lett.* **13**, 3942–3946 (2013). doi:10.1021/nl402062j Medline
39. K. F. Mak, M. Y. Sfeir, Y. Wu, C. H. Lui, J. A. Misewich, T. F. Heinz, Measurement of the optical conductivity of graphene. *Phys. Rev. Lett.* **101**, 196405 (2008). doi:10.1103/PhysRevLett.101.196405 Medline
40. P. Cueva, R. Hovden, J. A. Mundy, H. L. Xin, D. A. Muller, Data processing for atomic resolution electron energy loss spectroscopy. *Microsc. Microanal.* **18**, 667–675 (2012). doi:10.1017/S1431927612000244 Medline
41. Z. G. Gu, L. Heinke, C. Wöll, T. Neumann, W. Wenzel, Q. Li, K. Fink, O. D. Gordan, D. R. T. Zahn, Experimental and theoretical investigations of the electronic band structure of metal-organic frameworks of HKUST-1 type. *Appl. Phys. Lett.* **107**, 183301 (2015). doi:10.1063/1.4934737
42. C. Chen, T. Joshi, H. Li, A. D. Chavez, Z. Pedramrazi, P.-N. Liu, H. Li, W. R. Dichtel, J.-L. Bredas, M. F. Crommie, Local electronic structure of a single-layer porphyrin-containing covalent organic framework. *ACS Nano* **12**, 385–391 (2018). doi:10.1021/acsnano.7b06529 Medline
43. J. Als-Nielsen, D. McMorrow, Elements of modern X-ray physics (Wiley, 2011).
44. L. Cao, Z. Lin, F. Peng, W. Wang, R. Huang, C. Wang, J. Yan, J. Liang, Z. Zhang, T. Zhang, L. Long, J. Sun, W. Lin, Self-supporting metal-organic layers as single-site solid catalysts. *Angew. Chem. Int. Ed.* **55**, 4962–4966 (2016). doi:10.1002/anie.201512054 Medline
45. E.-Y. Choi, C. A. Wray, C. Hu, W. Choe, Highly tunable metal–organic frameworks with open metal centers. *CrystEngComm* **11**, 553–555 (2009). doi:10.1039/B819707P

ACKNOWLEDGMENTS

We thank D.V. Talapin and J. S. Anderson for helpful discussions. We thank S. E. Kim for helping with preparing the manuscript. We thank Zhan Zhang for helping with the XRR measurements. **Funding:** This work was primarily supported by the Air Force Office of Scientific Research (FA9550-16-1-0031, FA9550-16-1-0347, and FA9550-18-1-0480) and the National Science Foundation (NSF) through the University of Chicago Materials Research Science and Engineering Center (MRSEC; NSF DMR-1420709). Additional funding was provided by the Cornell Center for Materials Research (NSF DMR-1719875) and the Platform for the Accelerated Realization, Analysis, and Discovery of Interface Materials (PARADIM; NSF DMR-1539918). Material characterizations including electron microscopy were supported by the Cornell Center for Materials Research (NSF DMR-1719875) and the MRSEC Shared User Facilities at the University of Chicago (NSF DMR-1420709). Funding was provided by the National Science Foundation Grant Nos. NSF-CHE-1566364 and NSF-CHE-1900188 for UHV-STM imaging and instrumentation. This work made use of the Pritzker Nanofabrication Facility at the University of Chicago, which receives support from Soft and Hybrid Nanotechnology Experimental (SHyNE) Resource (NSF ECCS-1542205), a node of the National Science Foundation's National Nanotechnology Coordinated Infrastructure. Y.Z. acknowledges support by the Camille and Henry Dreyfus Foundation, Inc. under the Dreyfus Environmental Postdoc award EP-16-094. F.M. acknowledges support by the National Science Foundation Graduate Research Fellowship Program under Grant No. DGE-1746045. A.J.M. was supported by the Kadanoff-Rice Postdoctoral Fellowship through the University of Chicago MRSEC. This research used resources of the Advanced Photon Source, a U.S. Department of Energy (DOE) Office of Science User Facility operated for the DOE Office of Science by Argonne National Laboratory under Contract No. DE-AC02-06CH11357. **Author contributions:** Y.Z., B.C., and J.P. conceived the experiments. Y.Z. developed the LAP synthesis. B.C. fabricated the 2DP/TMD heterostructures, the capacitor devices, conducted GIXRD simulation, and performed the GIWAXS measurements. Y.Z. and B.C. grew the 2DP films, fabricated 2DP heterostructures, conducted AFM and SEM imaging, and performed the device measurements. Y.Z., B.C., and J.L. carried out the optical characterizations, C.P. and F.M. synthesized monolayer TMD films. A.R. and D.A.M. conducted TEM imaging, STEM imaging and FIB milling. S.B. and S.J.S. conducted STM imaging. Y.Z., B.C., H.Z., J.S., and F.M. performed the GIXRD experiments and the structural characterizations. K.L., K.K., A.J.M., and B.C. developed the stacking methods. Y.Z., B.C., and J.P. wrote the manuscript. All authors discussed and commented on the manuscript. **Competing interests:** The authors declare no competing financial interests. **Data and materials availability:** All data are reported in the main text and supplementary materials.

SUPPLEMENTARY MATERIALS

science.sciencemag.org/cgi/content/full/science.aax9385/DC1
Materials and Methods
Supplementary Text
Figs. S1 to S20
Table S1 to S3
References (*35–45*)
Movies S1 to S3

6 May 2019; accepted 28 October 2019
Published online 7 November 2019
10.1126/science.aax9385

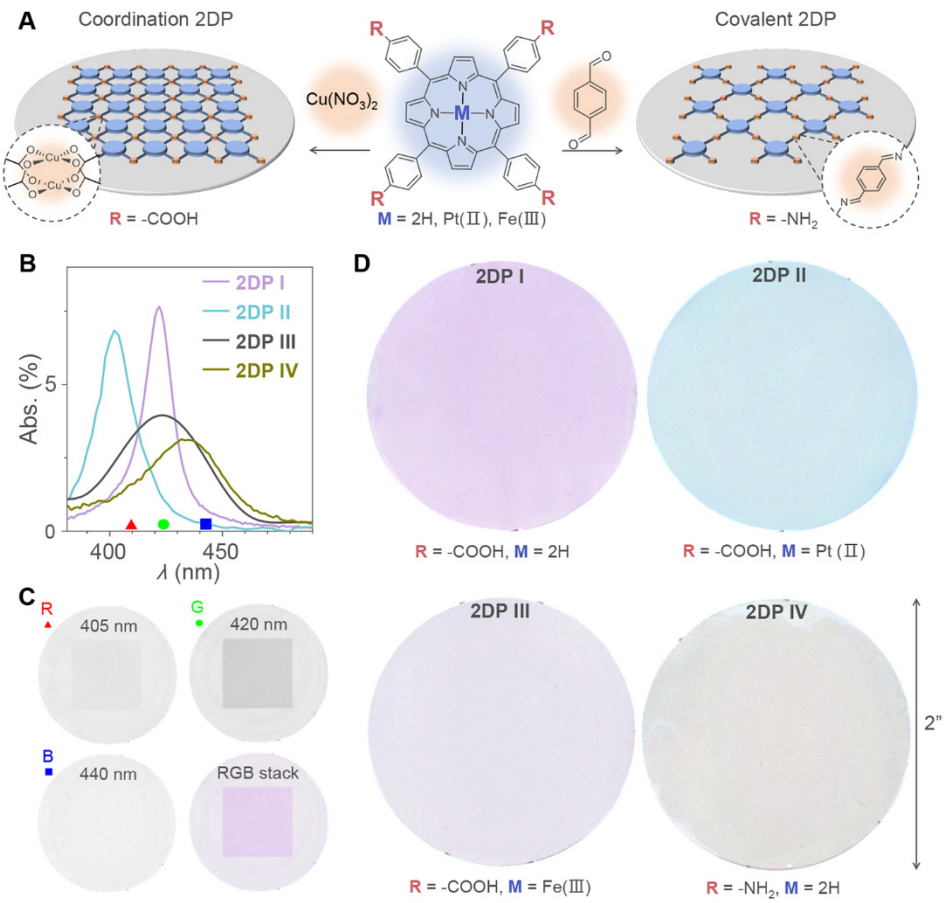

Fig. 1. Fig. 1. Wafer-scale monolayer 2DPs. (A) Schematic of monolayer 2DPs and corresponding chemical structures of the molecular precursors. (B) Absorption spectra of monolayer 2DPs on fused silica substrates. (C) Hyperspectral transmission images and resulting false color images of 1 inch-square 2DP I on a 2-inch fused silica substrate. Transmission images taken at the wavelength of 405 nm, 420 nm, and 440 nm are assigned as red, green and blue channel, respectively, to generate the false color image. A linear transmission scale of 50% to 95% was applied to all of the channels. (D) False color images of monolayer 2DPs covering entire 2-inch fused silica wafers. Same color code was applied in (C) and (D).

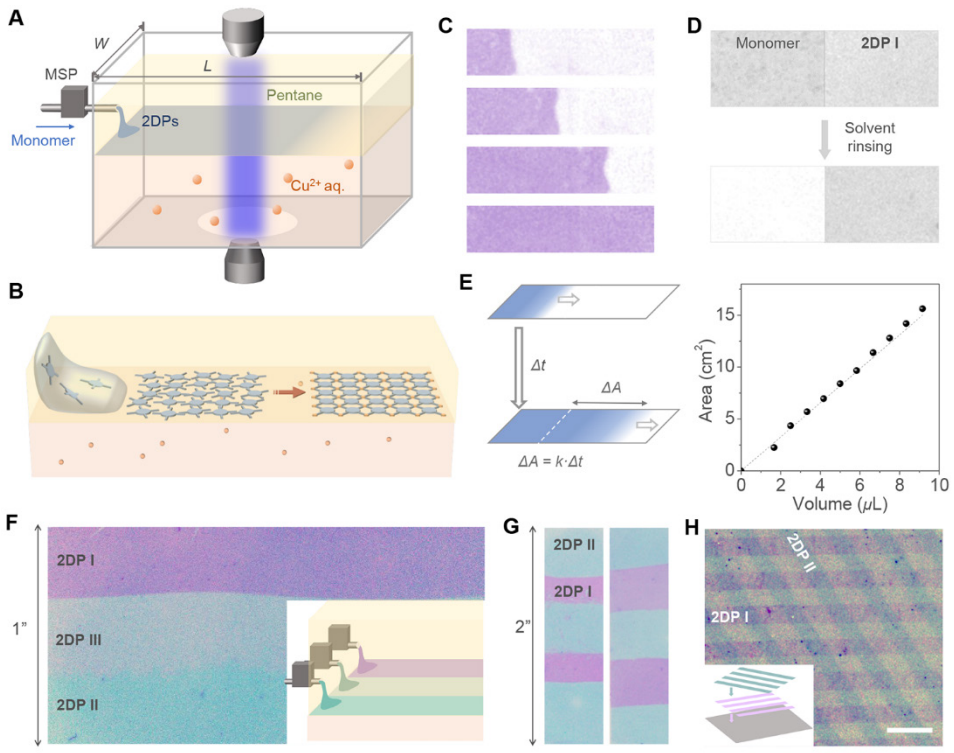

Fig. 2. Laminar assembly polymerization. (**A**) Schematic of a LAP reactor and in situ optical characterization apparatus. MSP stands for micro-syringe pump. (**B**) Schematic of the LAP synthesis that involves three phases. (**C**) False color images of **2DP I** film at four different stages during the growth. Images are individual frames extracted from Movie S2 measured at the wavelength of 425 nm. The precursor was injected from the left side. The film was colored with purple. The view size is 6 mm by 24 mm. (**D**) Optical transmission images comparing monolayer films produced with and without Cu^{2+} ions before and after rinsing measured at the wavelength of 425 nm. Image size is 0.67 cm by 1 cm. **(E)** Left: Schematic of a linear growth model based on LAP. The film area increases linearly over time with a rate constant $k = C_N \cdot A_0 \cdot v \cdot \eta / N_{eff}$, where C_N is number concentration of the molecular precursor, A_0 is unit cell area of **2DP I** lattice, v is volumetric injection rate, η is monomer-to-monolayer yield, and N_{eff} is effective layer number. Right: the relation between film area and volume of the injected precursor measured for **2DP I**. The dashed line indicates the theoretical curve for 100% monomer-to-monolayer conversion based on the lattice structure of **2DP I** (η = 100%, N_{eff} = 1). The data points were collected from Movie S3. **(F)** False color image of **2DP I/2DP III/2DP II** lateral junctions. Inset: schematic of generating lateral heterostructures of **2DP I/2DP III/2DP II** using three nozzles in LAP. (**G**) False color images of **2DP I/2DP II** lateral junctions with tunable stripe widths. (**H**) False color image of overlapped **2DP I** and **2DP II** stripes. Scale bar: 500 μm.

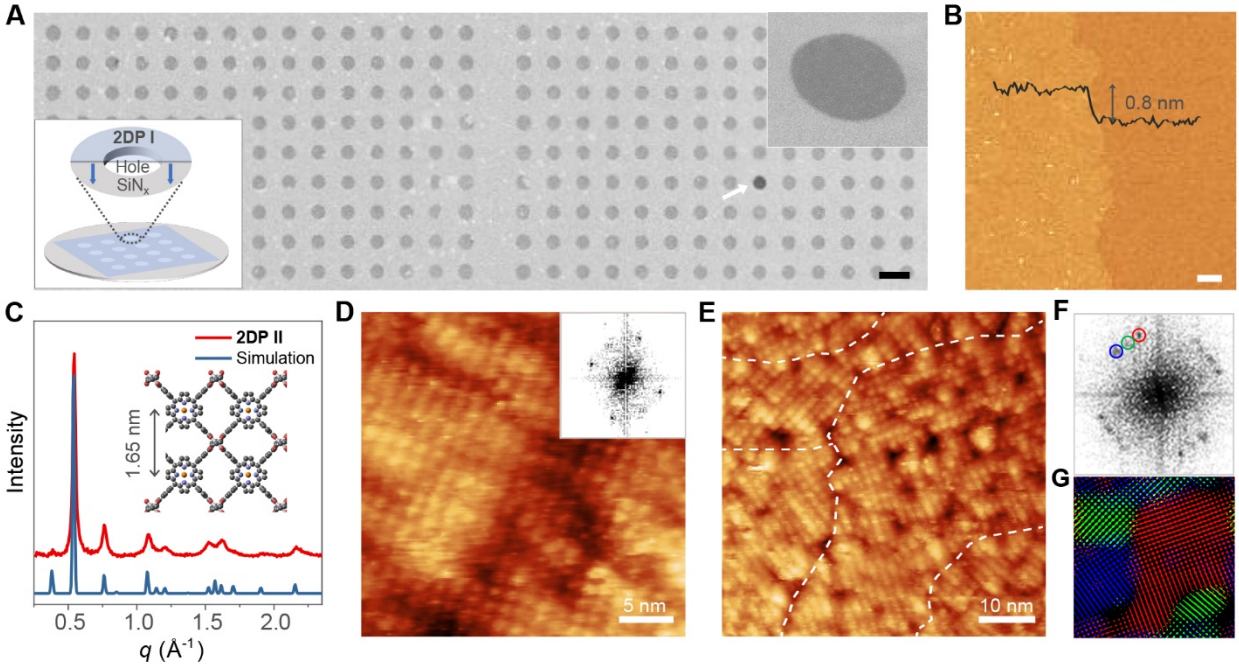

Fig. 3. Structural characterizations of 2DPs. (**A**) SEM image of monolayer **2DP I** on a holey silicon nitride TEM grid. The white arrow indicates a hole not covered by monolayer **2DP I**. Scale bar: 5 μm. Bottom-left inset: schematic of monolayer **2DP I** suspended over a hole on a silicon nitride TEM grid. Top-right inset: magnified SEM image of monolayer **2DP I** suspended over a 2 μm hole. (**B**) AFM height image of monolayer **2DP I**. Scale bar: 500 nm. Inset: AFM height profile. (**C**) Experimental and calculated in-plane XRD profiles for **2DP II**. The experiment was conducted on a stacked **2DP II** of 147 layers on sapphire. Inset: crystal structure of **2DP II**. (**D**) Constant-current STM topography image of a single crystalline domain of monolayer **2DP II** on a thin film of Au(111) on mica. Inset: 2D FFT of the image. (**E**) Constant-current STM topography image of multiple crystalline domains of monolayer **2DP II**. Boundaries between different domains are manually identified in white dashed line. (**F**) 2D FFT of (E) showing square lattices of three major orientations. (**G**) Color-coded inverse 2D FFT image generated using the three sets of square lattice spots in (F). One spot from each set is circled with the corresponding color in (F).

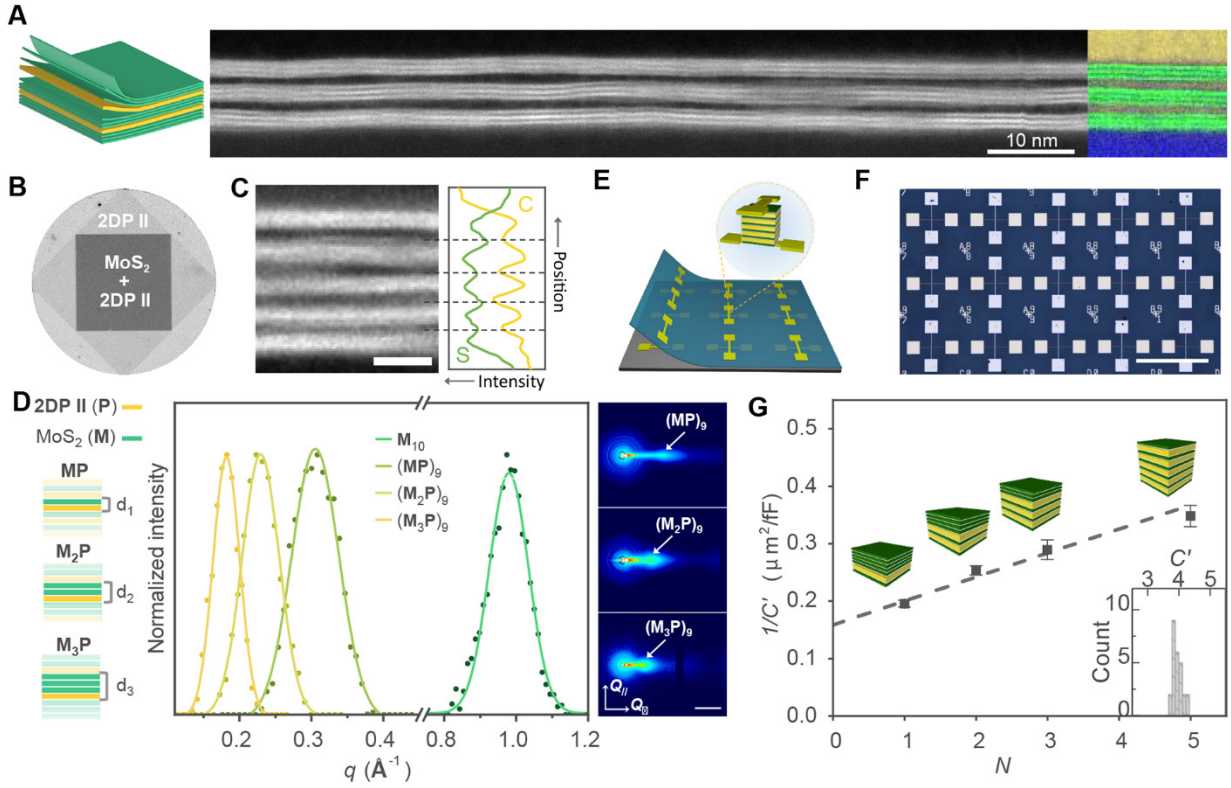

Fig. 4. 2DP/TMD vertical superlattices. (A) Left: schematic of a 2DP/$(MoS_2)_3$ superlattice. Middle: cross-sectional ADF STEM image of a **2DP II**/$(MoS_2)_3$ superlattice film transferred onto a SiO_2/Si substrate. Each bright band consists of three MoS_2 monolayers and each dark layer between the bands is a monolayer **2DP II**. Right: a composite image of carbon (Yellow) and oxygen (Blue) EELS mapping and ADF STEM signal (Green) taken from a different area on the sample shown in fig. S16. (B) Optical transmission image of a **2DP II**/MoS_2 heterostructure on fused silica taken at the wavelength of 405 nm. The diameter of the wafer is 1 inch. (C) Left: cross-sectional ADF STEM image of a **2DP III**/$(MoS_2)_2$ superlattice film transferred onto a SiO_2/Si substrate. Each bright layer consists of 2 layers of MoS_2 stacked and each dark layer is a **2DP III** monolayer. Right: the EELS profiles of carbon and sulfur taken from a different area on the sample shown in fig. S16. Scale bar: 5 nm. **(D)** Left: structures of **2DP II**/$(MoS_2)_n$ vertical superlattices. Middle: normalized diffraction peaks corresponding to **2DP II** /$(MoS_2)_n$ superlattices measured by GIWAXS. Right: 2D GIWAXS scattering patterns of **2DP II**/$(MoS_2)_n$ superlattices. Scale bar: 0.2 $Å^{-1}$. **(E)** Schematic of vertical capacitor device arrays and individual device geometry. **(F)** Optical image of a 3 by 5 capacitor device array. Scale bar: 500 μm. **(G)** Reciprocal of area-normalized capacitance, *1/C'*, as a function of *N*, number of **2DP II** layers in stacked $(MoS_2$/**2DP II**$)_N(MoS_2)_{6-N}$ films. Each data point is averaged from ten devices with corresponding stacked film structures shown above. Green: MoS_2; yellow: **2DP II**. Inset shows a capacitance histogram of 25 devices of $N = 2$.

Wafer-scale synthesis of monolayer two-dimensional porphyrin polymers for hybrid superlattices

Yu Zhong, Baorui Cheng, Chibeom Park, Ariana Ray, Sarah Brown, Fauzia Mujid, Jae-Ung Lee, Hua Zhou, Joonki Suh, Kan-Heng Lee, Andrew J. Mannix, Kibum Kang, S. J. Sibener, David A. Muller and Jiwoong Park

published online November 7, 2019